

Elastic FWI for large impedance contrasts

Zedong Wu*, Zhiyuan Wei, Zhigang Zhang, Jiawei Mei, Rongxin Huang, and Ping Wang (CGG)

Summary

Recent advances in full-waveform inversion (FWI) algorithms have allowed it to work stably and effectively in different geological settings, especially in areas with geobodies of large impedance contrasts such as salt, despite its presently taken acoustic assumption. This has resulted in a leap in salt velocity model building over the conventional interpretation-driven approach, providing significantly improved salt models and a step-change in subsalt imaging. Furthermore, it produces a directly interpretable FWI Image, the normal derivative of the FWI velocities, that is now widely accepted as another step-change for subsalt imaging. However, elastic effects at the large impedance contrasts cause smearing of the salt boundary and a considerable salt halo in acoustic FWI results. To mitigate this issue, we have incorporated an elastic modeling engine into our acoustic Time-lag FWI algorithm (A-TLFWI) that has proven effective in mitigating the negative impact of large differences between synthetic and real data at sharp contrasts. Elastic TLFWI (E-TLFWI) can model the energy at large impedance contrasts with better amplitudes and phases. This intrinsically reduces data mismatch between synthetic and real data and thus further improves the convergence. Using an ocean bottom node (OBN) data set in the Gulf of Mexico (GoM), we demonstrate that E-TLFWI can significantly reduce the salt halo that typically occurs in A-TLFWI. Although it does not change the model kinematics much compared to A-TLFWI, as evident in RTM images, it provides FWI Images of more balanced amplitudes, improved focusing, and higher signal-to-noise ratio (S/N).

Introduction

Full-waveform inversion (Lailly, 1983; Tarantola, 1984) provides a natural and elegant way to automatically build the Earth model through inversion of recorded full-wavefield data. However, successful FWI application in areas of large impedance contrasts, such as salt, has remained challenging for over thirty years. It was only recently that FWI finally fulfilled its promise for salt velocity model update and led to significant uplifts in subsalt imaging, despite its acoustic nature (Shen et al., 2017; Michell et al., 2017; Zhang et al., 2018; Wang et al., 2019; Nolte et al., 2019). Obtaining an accurate salt model does not solve the complete puzzle yet; subsalt imaging is still often troubled by illumination issues that are difficult to resolve with conventional migration methods that use primary reflections only. Noticing that the illumination issue can be better mitigated by utilizing the full-wavefield data, including transmission waves, primary reflections, and their multiples, we propose FWI Imaging to realize full-wavefield imaging through least-squares fitting of the full-wavefield data (Zhang et al., 2020; Huang et al., 2021). We demonstrate that FWI could be extended to produce the FWI velocity and FWI Image in one inversion. Not only do FWI Images produce comparable structures to those of conventional migration images, but they also provide appealing benefits such as better amplitude

balance, event continuity, and higher resolution, especially in areas of poor illumination, marking another step-change in subsalt imaging (Zhang et al., 2020; Huang et al., 2021; Wei et al., 2021).

Despite the widespread success of acoustic FWI, the missing elasticity may result in non-negligible effects in current FWI results. For example, elastic effects from the large impedance contrasts can smear the salt boundary and result in a salt halo considerably larger than what we would expect from the resolution limit at the inversion frequency. Although the salt halo, which appears as a smoothing effect of the salt boundary, inflicts little adverse impact on the overall model kinematics and, thus, the migration image focusing, it does pose a problem for direct interpretation of the FWI velocity and FWI Image around salt bodies. Additionally, the salt halo could have a more pronounced effect on the model kinematics in areas close to steep salt flanks or where salt bodies become small.

Mora and Wu (2018) use synthetic examples to demonstrate that, even in marine settings, accounting for elastic effects is important. Agudo et al. (2020) propose using filters derived from matching elastic modeled data to acoustic modeled data to compensate for the elastic effects in acoustic FWI. However, accurately compensating for elastic effects in shot gathers is a very challenging task, especially in complex geological settings. Plessix and Krupovnickas (2021) implement elastic waveform inversion to illustrate its potential benefits for salt model updates using long-offset, low-frequency seismic data. Nonetheless, the improvements to velocity models and migration images from elastic FWI appear to be smaller than expected, making it difficult to justify the significantly increased cost.

We developed an elastic FWI built on top of our proven acoustic Time-lag FWI algorithm (Zhang et al., 2018; Wang et al., 2019). With an elastic modeling engine, the modeled reflection and transmission energies at large impedance contrasts have amplitudes and phases that better match the recorded data, which effectively reduces data misfits and improves the convergence. As a result, the salt halo is significantly reduced in the E-TLFWI velocity model, and the resulting FWI Image has more balanced amplitudes, better continuity, and higher S/N compared with its acoustic counterpart.

Method

The three largest challenges to the success of FWI are cycle-skipping, amplitude discrepancy between synthetic and recorded data, and insufficient physics in the modeling engine. We propose to combine an elastic modeling engine with a time-lag cost function to tackle these challenges.

We first define the stress vector as

$$\sigma = (\sigma_{11}, \sigma_{22}, \sigma_{33}, \sigma_{23}, \sigma_{13}, \sigma_{12})^T$$

Elastic FWI for large impedance contrasts

and the strain vector as

$$\epsilon = (\epsilon_{11}, \epsilon_{22}, \epsilon_{33}, \epsilon_{23}, \epsilon_{13}, \epsilon_{12})^T.$$

Hooke's law for linear elastic material can be written as

$$\sigma = C\epsilon, \quad (1)$$

where C is the stiffness matrix of material parameters. In the case of orthorhombic media, C can be written as

$$C = \begin{pmatrix} c_{11} & c_{12} & c_{13} & 0 & 0 & 0 \\ c_{12} & c_{22} & c_{23} & 0 & 0 & 0 \\ c_{13} & c_{23} & c_{33} & 0 & 0 & 0 \\ 0 & 0 & 0 & c_{44} & 0 & 0 \\ 0 & 0 & 0 & 0 & c_{55} & 0 \\ 0 & 0 & 0 & 0 & 0 & c_{66} \end{pmatrix}.$$

Following Tsvankin (1997), we introduce the model parameterization system:

$$c_{11} = \rho(1 + 2\varepsilon_2)v_p^2, c_{22} = \rho(1 + 2\varepsilon_1)v_p^2, c_{33} = \rho v_p^2,$$

$$c_{44} = \rho \frac{1 + 2\gamma_1}{1 + 2\gamma_2} v_s^2, c_{55} = \rho v_s^2, c_{66} = \rho(1 + 2\gamma_1)v_s^2,$$

where, v_p and v_s are vertical P-wave and S-wave velocities, respectively, and

$$c_{12} = \sqrt{c_{11} - c_{66}} \sqrt{(1 + 2\delta_3)c_{11} - c_{66}} - c_{66},$$

$$c_{13} = \sqrt{c_{33} - c_{55}} \sqrt{(1 + 2\delta_2)c_{33} - c_{55}} - c_{55},$$

$$c_{23} = \sqrt{c_{33} - c_{44}} \sqrt{(1 + 2\delta_1)c_{33} - c_{44}} - c_{44}.$$

We next define the derivative matrix D as

$$D = \begin{pmatrix} \partial_1 & 0 & 0 & 0 & \partial_3 & \partial_2 \\ 0 & \partial_2 & 0 & \partial_3 & 0 & \partial_1 \\ 0 & 0 & \partial_3 & \partial_2 & \partial_1 & 0 \end{pmatrix}.$$

The elastic wave equation can be then described as

$$\rho \partial_{tt}^2 u = D^T \sigma, \quad (2)$$

where, $u = (u_1, u_2, u_3)^T$ is the displacement vector. Based on the small strain assumption, strain ϵ and displacement vector u have the following linear relationship:

$$\epsilon = Du. \quad (3)$$

Combining Equations (1), (2), and (3), we can obtain the second-order equation of stress:

$$\partial_{tt}^2 \sigma = CD \left(\frac{1}{\rho} D^T \sigma \right). \quad (4)$$

After deriving the stress vector σ from Equation (4), we can compute the pressure data as

$$p = (\sigma_{11} + \sigma_{22} + \sigma_{33})/3. \quad (5)$$

With a time-lag cost function, A-TLFWI proves to be effective in mitigating cycle-skipping and amplitude-discrepancy issues. We can simply incorporate this elastically modeled synthetic data p into the time-lag cost function (Luo and Schuster, 1991; Zhang et al., 2018) for E-TLFWI:

$$J(d, p) = \sum_{s,r,w} c(\Delta\tau) \Delta\tau^2, \quad (6)$$

where $\Delta\tau$ is the traveltime difference between real data d and synthetic data p :

$$\Delta\tau = \operatorname{argmax}_\tau \int_{t_1}^{t_2} d(t + \tau)p(t)dt.$$

And $c(\Delta\tau)$ is defined as the cross-correlation coefficients between the recorded data and synthetic data:

$$c(\Delta\tau) = \frac{\int_{t_1}^{t_2} d(t + \Delta\tau)p(t)dt}{\sqrt{\int_{t_1}^{t_2} d(t + \Delta\tau)^2 dt \int_{t_1}^{t_2} p(t)^2 dt}}.$$

E-TLFWI can theoretically invert for both v_p and v_s . However, in practice, to avoid the crosstalk of multi-parameter inversion, the inverting variable is often only v_p , with v_s set fixed or updated with v_p based on a pre-defined relationship. Like the case of A-TLFWI, E-TLFWI can also be extended to produce an elastic FWI Image, the normal derivative of P-wave impedance I , assuming a smoothly varying density model (Zhang et al., 2020):

$$\frac{\partial I}{\partial n} \approx \rho (\sin \theta \cos \varphi \partial_x v_p + \sin \theta \sin \varphi \partial_y v_p + \cos \theta \partial_z v_p),$$

where θ and φ are the structure dip angle and azimuth angle, respectively.

In the next section, we begin with a comparison of synthetic data modeled by acoustic and elastic modeling engines in the presence of large impedance contrasts to illustrate why an elastic modeling engine is necessary in such cases. Next, we demonstrate the effectiveness of E-TLFWI using an OBN data set in the Gulf of Mexico (GoM).

Synthetic and field data examples

To start, we examine the difference between acoustic and elastic modeling at a large impedance contrast with a two-layer synthetic test. Figures 1a and 1d show the synthetic shot gather modeled by an acoustic and an elastic engine, respectively. The wiggle display of the zoomed-in section, marked by the purple rectangle in Figures 1a and 1d, clearly shows the phase difference between the acoustic and elastic engines (Figures 1b

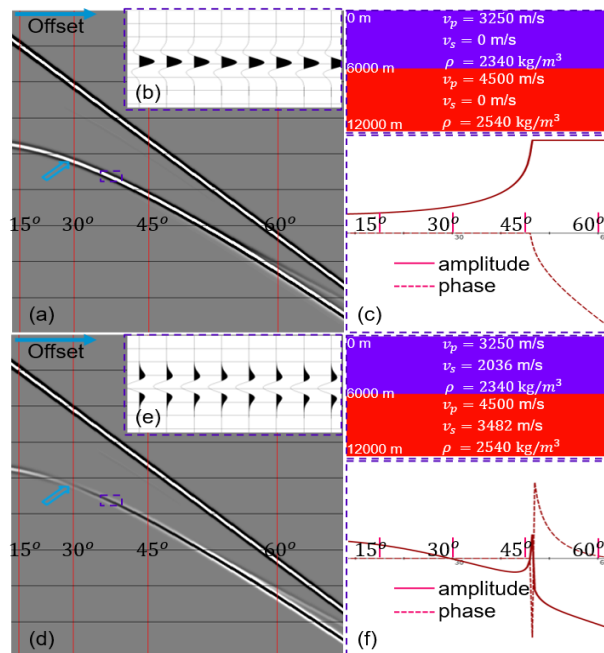


Figure 1: Synthetic comparison of two-layer model. Synthetic traces from (a) acoustic engine and (d) elastic engine. (b) and (e) show the zoomed-in displays for the rectangular region. (c) and (f) show the analytic amplitude and phase from acoustic and elastic propagation.

and 1e). The difference in this simple example can be validated by the analytical solution (Figures 1c and 1f). This difference creates a systematic data mismatch for the strong reflection energy from large impedance contrasts in acoustic FWI using field data, which in turn gives artificial velocity updates around the sharp boundary. We believe this is the main reason A-TLFWI often suffers from salt halos for field data examples in salt settings.

Our field data example uses OBN data from the Herschel field in Mississippi Canyon, GoM. A-TLFWI with this OBN data set has resulted in significant improvements in velocity model and RTM image quality over the conventional top-down velocity model building workflow (Yao et al., 2020). However, the salt halo of the 15 Hz A-TLFWI velocity model is apparent (Figures 2a and 2c). When we run E-TLFWI to the same frequency of 15 Hz (Figures 2b and 2d), the salt halo of the E-TLFWI model is considerably reduced compared with the one in the A-TLFWI velocity model, which indicates that the elastic effects have significant impact on the sharpness of the inverted salt boundaries in addition to the inversion frequency. The sharpened salt boundaries around the steeply dipping salt flank in the E-TLFWI model can be better observed in the zoomed-in displays in Figures 2c and 2d. Besides sharper salt boundaries, the E-TLFWI model also has clearer velocity contrasts and better details in the sediment and subsalt areas than the A-TLFWI model.

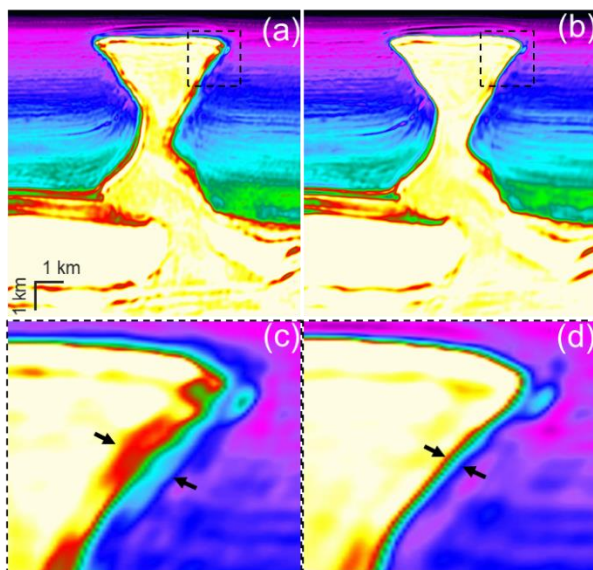


Figure 2: Section view of velocity models from the Herschel OBN data. (a) 15 Hz A-TLFWI velocity model and (b) 15 Hz E-TLFWI velocity model. (c) and (d) are the zoomed-in displays of the black dashed rectangles in (a) and (b). E-TLFWI model shows sharpened salt boundaries and improved velocity details in sediments.

Despite the improved velocity model with E-TLFWI (Figures 3a and 3d), acoustic RTM images with the acoustic and elastic TLFWI velocity models exhibit similar quality (Figures 3b and 3e). The only slight improvements in the RTM images are observed in the area right below the steep salt flank, where the

reduced salt halo in the E-TLFWI model has a more appreciable effect on the kinematics. The zone directly below the salt remains dim with low S/N in the RTM image with the E-TLFWI model, likely due to poor illumination in this local area. Meanwhile, the acoustic FWI Image (Figure 3c) shows more balanced amplitudes and improved event continuity compared to both RTM images (Figures 3b and 3e) in the dim-amplitude zone. However, the events in the acoustic FWI Image right below the base of salt (BOS) still have cross-cutting noise parallel to the BOS. Additionally, the subsalt events right below the BOS are not clearly imaged since they are masked by the salt halo (Figure 3g). In contrast, the elastic FWI Image better reveals the reflectors around and below salt with more balanced amplitudes and improved continuity (Figure 3f). Similar observations can be made on the depth views at two different depths (Figures 4), where the events closer to the salt diapir (highlighted by the ellipses) show higher S/N and better continuity in the E-TLFWI Images than the A-TLFWI Images. Moreover, the faults are also better defined in the E-TLFWI Images.

Discussion

The E-TLFWI velocity model from the Herschel OBN data has notably reduced salt halos compared with its acoustic counterpart (Figures 2). Still, the uplifts from RTM using the A-TLFWI velocity compared to that using the E-TLFWI velocity are far less impressive (Figures 3b and 3e). This is not very surprising since RTM as a migration approach is largely determined by the kinematic information contained in the low wavenumbers of the velocity model. Even though high-wavenumber details in the velocity, such as the sharpness of salt boundaries, can introduce small kinematic errors, their effects on subsalt images are barely observable in RTM images because RTM is susceptible to other more dominant problems such as poor illumination. In other words, even if the propagation engine is upgraded from acoustic to elastic, RTM and other migration-based approaches may still not be good enough to appreciate the full benefits of high-wavenumber details in elastic FWI velocity models.

FWI Imaging (Zhang et al., 2020; Huang et al., 2021), which utilizes the full-wavefield data, applies least-squares data fitting from low to high frequencies, and derives a velocity and an image in one consistent inversion, has been proven to provide greatly improved structural images when compared with RTM. We can see that the acoustic FWI Image (Figure 3c) is considerably better than RTM (Figure 3b) using the same acoustic FWI velocity model, and the elastic FWI Image (Figure 3f) is considerably better than RTM (Figure 3e) using the same elastic FWI velocity model. Moreover, compared to the A-TLFWI Image (Figure 3c), the E-TLFWI Image (Figure 3f) has more balanced amplitudes, improved event continuity, and higher S/N, which should significantly reduce the uncertainty in reservoir interpretation. Finally, with this more advanced imaging approach, we can now witness the long-expected imaging benefits from elastic FWI that are worth the considerably increased compute cost over acoustic FWI.

Elastic FWI for large impedance contrasts

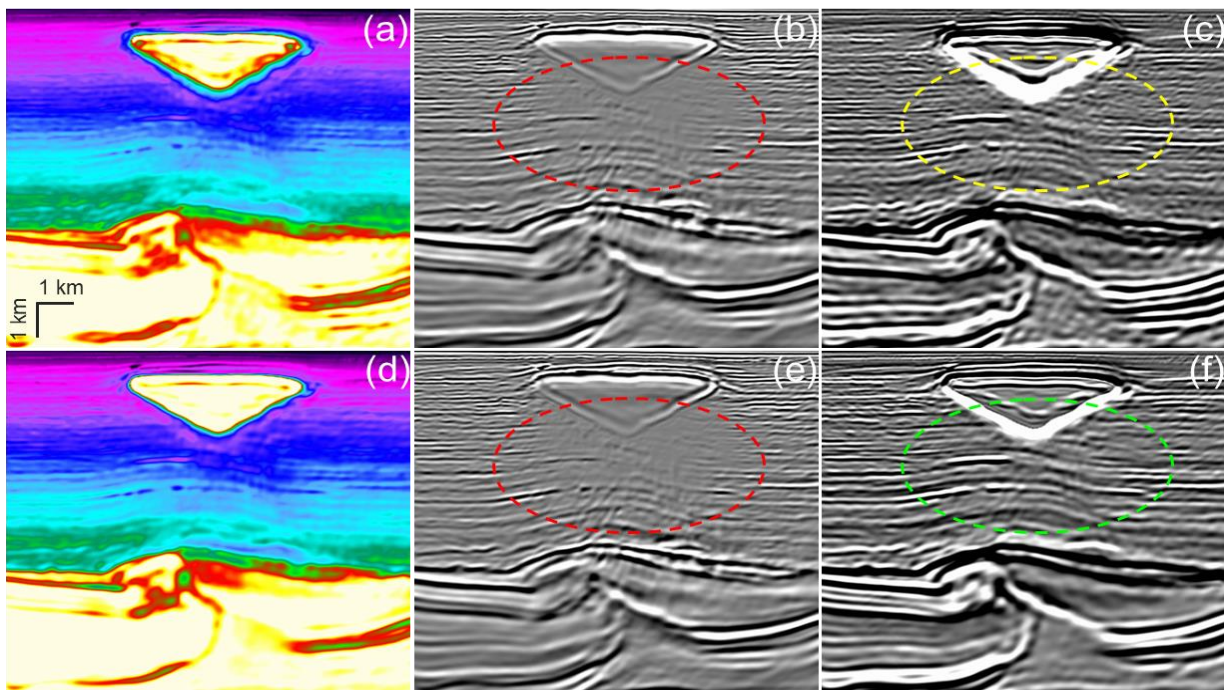


Figure 3: Section views of (a) 15 Hz A-TLFWI model, (b) 15 Hz acoustic RTM image migrated with A-TLFWI model, (c) 15 Hz acoustic FWI Image and (d) 15 Hz E-TLFWI model, (e) 15 Hz acoustic RTM with E-TLFWI model, and (f) 15 Hz elastic FWI Image.

One major disadvantage of FWI Imaging is that it only provides stack images. In other words, it needs to be combined with other approaches to obtain common image gathers (CIGs) for post-migration elastic parameter inversion. Now, with our newly developed E-TLFWI, is it possible to directly invert for all the elastic parameters so that no CIGs are needed? Theoretically, E-TLFWI can be formulated to invert for any elastic parameters. However, in practice, there are a few major challenges in multi-parameter E-TLFWI, such as the strong coupling among different elastic parameters and insufficient constraints for all the parameters from the seismic data. Therefore, as of today, S-wave velocity is still mostly used as an auxiliary model to assist a better inversion of P-wave velocity. Further research is still needed to find inversion schemes that can better decouple different elastic parameters, workflows that can better utilize multi-component data (e.g., pressure data and three-component velocity data from OBN surveys), and new sensors and/or survey designs that can provide data with more constraints to the key elastic parameters for which we would like to invert.

Conclusions

Using a synthetic example, we illustrated that an elastic modeling engine is crucial for FWI to reduce the discrepancy between synthetic data and real data in the presence of large impedance contrasts. Next, using a field OBN data example in the GoM, we demonstrated that E-TLFWI can significantly reduce the salt halo, which is typically observed in A-TLFWI. Finally, we also showed that FWI Imaging is a more advanced imaging technology to appreciate the full benefits of E-TLFWI over standard migration approaches. Though the

improvements from the E-TLFWI model are barely observed in RTM images, FWI Images from E-TLFWI clearly show more balanced amplitudes, improved event continuity, and higher S/N than their acoustic counterparts.

Acknowledgments

We thank CGG for permission to publish this work. We also thank Yu Pu for his help with the synthetic study.

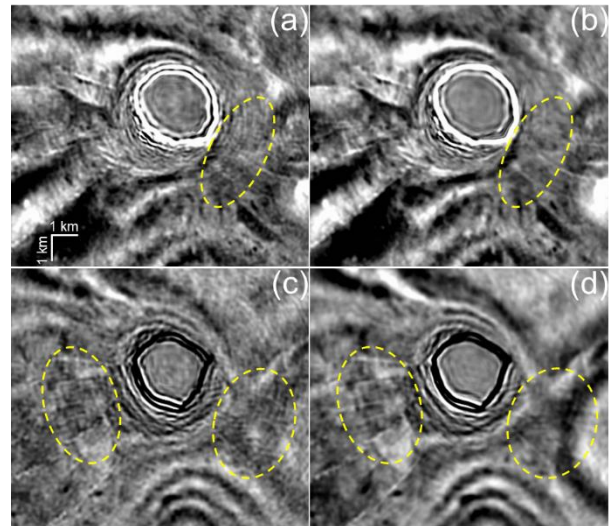


Figure 4: Depth view of FWI Images. (a)-(b) 15 Hz FWI Images from A-TLFWI and E-TLFWI at depth \sim 4 km. (c)-(d) 15 Hz FWI Images from A-TLFWI and E-TLFWI at depth \sim 5 km. FWI Images from E-TLFWI show higher S/N and improved details.

REFERENCES

- Agudo, O. C., N. V. da Silva, G. Stronge, and M. Warner, 2020, Mitigating elastic effects in marine 3-D full-waveform inversion: *Geophysical Journal International*, **220**, 2089–2104, doi: <https://doi.org/10.1093/gji/ggz569>.
- Huang, R., Z. Zhang, Z. Wu, Z. Wei, J. Mei, and P. Wang, 2021, Full-waveform inversion for full-wavefield imaging: Decades in the making: *The Leading Edge*, **40**, 324–334, doi: <https://doi.org/10.1190/tle40050324.1>.
- Lailly, P., 1983, The seismic inverse problem as a sequence of before stack migrations in Conference on inverse scattering: Theory and application: SIAM, 206–220.
- Luo, Y., and G. T. Schuster, 1991, Wave-equation traveltime inversion: *Geophysics*, **56**, 645–653, doi: <https://doi.org/10.1190/1.1443081>.
- Michell, S., X. Shen, A. Brenders, J. Dellinger, I. Ahmed, and K. Fu, 2017, Automatic velocity model building with Complex salt: Can computers finally do an Interpreter's job? 87th Annual International Meeting, SEG, Expanded Abstracts, 5250–5254, doi: <https://doi.org/10.1190/segam2017-17778443.1>.
- Mora, P., and Z. Wu, 2018, Elastic versus acoustic inversion for marine surveys: *Geophysical Journal International*, **214**, 596–622, doi: <https://doi.org/10.1093/gji/ggy166>.
- Nolte, B., F. Rollins, Q. Li, S. Dadi, S. Yang, J. Mei, and R. Huang, 2019, Salt velocity model building with FWI on OBN data: Example from Mad Dog, Gulf of Mexico: 89th Annual International Meeting, SEG, Expanded Abstracts, 1275–1279, doi: <https://doi.org/10.1190/segam2019-3216777.1>.
- Plessix, R.-E., and T. Krupovnickas, 2021, Low-frequency, long-offset elastic waveform inversion in the context of velocity model building: *The Leading Edge*, **40**, 342–347, doi: <https://doi.org/10.1190/tle40050342.1>.
- Shen, X., I. Ahmed, A. Brenders, J. Dellinger, J. Etgen, and S. Michell, 2017, Salt model building at Atlantis with full-waveform inversion: 87th Annual International Meeting, SEG, Expanded Abstracts, 1507–1511, doi: <https://doi.org/10.1190/segam2017-17738630.1>.
- Tarantola, A., 1984, Inversion of seismic reflection data in the acoustic approximation: *Geophysics*, **49**, 1259–1266, doi: <https://doi.org/10.1190/1.1441754>.
- Tsvankin, I., 1997, Anisotropic parameters and P-wave velocity for orthorhombic media: *Geophysics*, **62**, 1292–1309, doi: <https://doi.org/10.1190/1.1444231>.
- Wang, P., Z. Zhang, J. Mei, F. Lin, and R. Huang, 2019, Full-waveform inversion for salt: A coming of age: *The Leading Edge*, **38**, 204–213, doi: <https://doi.org/10.1190/tle38030204.1>.
- Wei, Z., J. Mei, Z. Wu, Z. Zhang, R. Huang, and P. Wang, 2021, FWI imaging: Revealing the unprecedented resolution of seismic data: First International Meeting for Applied Geoscience & Energy, SEG/AAPG, Expanded Abstracts, 682–686, doi: <https://doi.org/10.1190/segam2021-3583772.1>.
- Yao, Y., H. Zhang, L. Hu, and C. Peng, 2020, Improving Mississippi Canyon images with ocean bottom node data: Challenges and surprises: 90th Annual International Meeting, SEG, Expanded Abstracts, 661–665, doi: <https://doi.org/10.1190/segam2020-3423896.1>.
- Zhang, Z., J. Mei, F. Lin, R. Huang, and P. Wang, 2018, Correcting for salt misinterpretation with full-waveform inversion: 88th Annual International Meeting, SEG, Expanded Abstracts, 1143–1147, doi: <https://doi.org/10.1190/segam2018-2997711.1>.
- Zhang, Z., Z. Wu, Z. Wei, J. Mei, R. Huang, and P. Wang, 2020, FWI Imaging: Full-wavefield imaging through full-waveform inversion: 90th Annual International Meeting, SEG, Expanded Abstracts, 656–660, doi: <https://doi.org/10.1190/segam2020-3427858.1>.